Micromegas chambers for the ATLAS New Small Wheel upgrade

Jinst

Published by IOP Publishing for Sissa Medialab

Received: *May 19, 2020*
Accepted: *June 4, 2020*
Published: *September 4, 2020*

International Conference on Instrumentation for Colliding Beam Physics
Novosibirsk, Russia
24–28 February, 2020

Micromegas chambers for the ATLAS New Small Wheel upgrade

I. Gnesi on behalf of ATLAS Muon collaboration

Enrico Fermi Research Center - CREF
Rome, Italy
INFN LNF Cosenza Group
Cosenza, Italy

E-mail: ivan.gnesi@cref.it

Abstract: The ATLAS collaboration at LHC has chosen the resistive Micromegas technology, along with the small-strip Thin Gap Chambers (sTGC), for the high luminosity upgrade of the first muon station in the high-rapidity region, the so called New Small Wheel (NSW) project. After the R&D, design and prototyping phase, the series production Micromegas quadruplets are being constructed at the involved construction sites in France, Germany, Italy, Russia and Greece. At CERN, the final validation and the integration of the modules in Sectors are in progress. The installation of the first NSW, the NSW-A is foreseen for the LHC long shutdown in 2020. The construction of the four types of large size quadruplets, all having trapezoidal shapes with surface areas between 2 and 3 m^2, will be reviewed. The achievement of the requirements for these detectors revealed to be even more challenging than expected, when scaling from the small prototypes to the large dimensions. The encountered problems will be described, to a large extent common to other micro-pattern gaseous detectors, along with the adopted solutions. Final quality assessment and validation results on the achieved mechanical precision, on the High-Voltage stability during operation with and without irradiation will be reviewed together with the most relevant steps and results of the modules integration into sectors.

Keywords: Gaseous imaging and tracking detectors; Micropattern gaseous detectors (MSGC, GEM, THGEM, RETHGEM, MHSP, MICROPIC, MICROMEGAS, InGrid, etc)

https://doi.org/10.1088/1748-0221/15/09/C09019

Contents

2020 JINST 15 C09019

1 Introduction

The Large Hadron Collider (LHC) is presently undergoing a series of major upgrades. As soon as the second long shutdown (LS2) will be complete in 2020-21 the luminosity of the accelerator will reach 2–3 $\times$ 10^{34} cm^{-2} s^{-1}, while after LS3 we expect 5–7 $\times$ 10^{34} as target luminosity. The LHC luminosity upgrade is expected to allow its major experiments to collect up to 100 fb^{-1}/year of data. In order to take advantage of the LHC luminosity upgrade, the ATLAS [1] experiment is as well undergoing major upgrades, involving a complex section of the detector, the Muon Spectrometer (MS).

The MS is devoted to particle track reconstruction with high precision, while providing information to the Level-1 (L1) trigger. To this purpose the innermost stations of the forward region of the ATLAS MS (Small Wheel - SW) play a fundamental role. The present SW detector technologies, Thin Gap Chambers (TGC) and Monitorized Drift Tubes (MDT) are not capable of keeping the same performances at high luminosity. The SW covers the η range between 1.3 and 2.7, where at high luminosity the expected particle rate will be between 600 Hz/cm^2 and 15 kHz/cm^2. The MDT technology would undergo a strong efficiency loss and the present trigger scheme based on coincidences of TGC would provide a huge amount of fake triggers in the low energy muon region (figure 1, right plot). The excellent performances needed at high luminosity, demand for a momentum resolution better than 15 at $p_T \sim 1$ TeV within the Muon Spectrometer; to this purpose each track segment in the NSW needs to be reconstructed with a position resolution in the bending plane better than 50 µm. This parameter should not degrade even if a considerable fraction of the detected hits are linked to background particles or if some detector plane had to be temporarily excluded. These constraints bring to a stringent set of requirements: a spatial resolution better than 100 µm per detector layer and an angular resolution of 1 mrad for the online track segment reconstruction at the L1 trigger level.

These arguments [2] demanded for a new detector, the New Small Wheel (NSW), to replace the former one during the upgrade. In figures 1 and 2 the position of the NSW with respect to the ATLAS detector is shown.

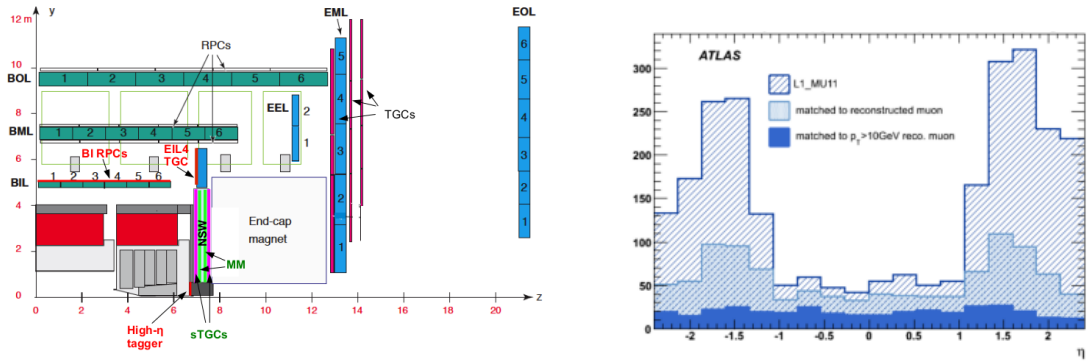

Figure 1. Left: position of a sector of the NSW in the ATLAS Detector (ZY projection). Right: fake trigger rate compared with the actually reconstructed muon tracks [2]. Copyright 2020 CERN for the benefit of the ATLAS Collaboration. CC-BY-4.0 license.

The NSW detector will be composed by two wheels. Each wheel hosts two different kind of detector technologies: the Micromegas (MM) and the small Thin Gap Chambers (sTGC). The sTGC [3] will be primarily devoted to the L1 trigger functions, while providing also tracking information. The MM [4] will be dedicated to precision tracking; it will also provide information on track segments found by the muon end-cap middle stations, improving the trigger capabilities.

In figure 3 the fine structure of a NSW wheel is shown. The two technologies will be overlapping in the fundamental unit of a NSW wheel: a sector. Each wheel will be composed by eight large and eight small sectors. Each sector hosts two wedges (WE) per detector technology. Each of the 16 sectors will be equipped by a sandwich configuration of four WE sTGC-MM-MM-sTGC. A MM WE is composed by two modules, SM1 and SM2 for the small WEs and LM1 and LM2 for the large WEs. Each module is a quadruplet, thus providing 4 detection layers through the detector thickness, for position measurements in the radial (precision) and in the azimuthal coordinates. This structure allows each sector to provide a total of 16 active layers through the Z coordinates. The sTGC-MM combination make up a fully redundant detector system for triggering and tracking with both online and offline functions.

The NSW MM detectors will cover an active area of 1280 m^2. The whole MM structure will include 128 detectors, in total more than 2×10^6 channels.

The specific features of a MM layer and its layout will be discussed in section 2.

2 Detector layout and the resistive strip technology

The MM technology was chosen because of its excellent capabilities, fulfilling the requirements of the high luminosity phase. The MM are micro-pattern gaseous detectors with high rate capability and good performances in terms of efficiency, spatial and time resolutions.

2020 JINST 15 C09019

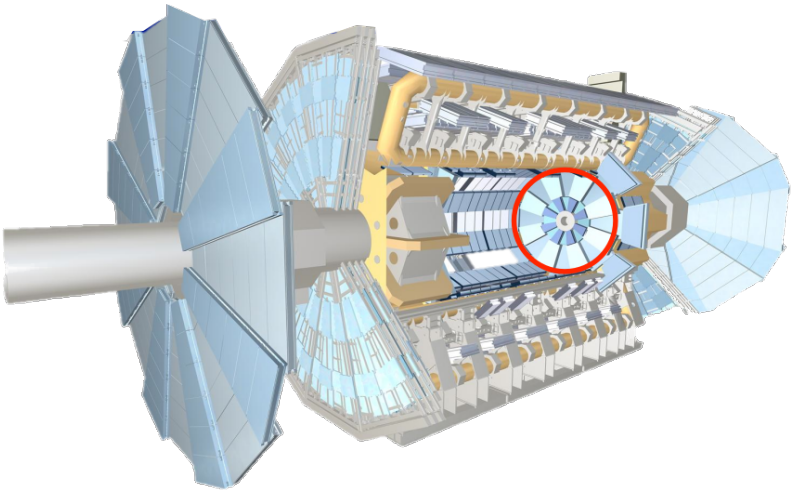

Figure 2. The NSW position within the forward region of the ATLAS Muon Spectrometer. Copyright 2020 CERN for the benefit of the ATLAS Collaboration. CC-BY-4.0 license.

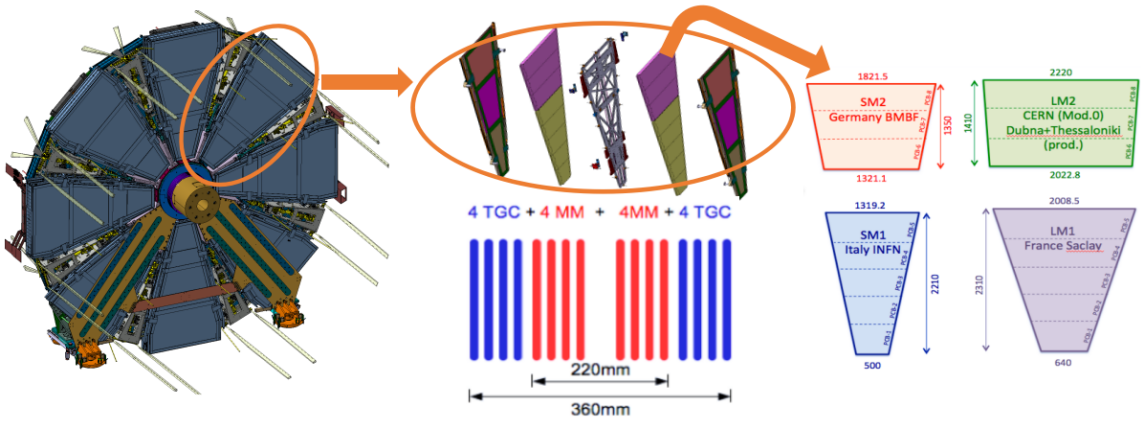

Figure 3. The structure of the NSW. Left: a 3D drawing of the NSW. Center-Top: the sandwich structure of a sector, hosting two sTGC WE and two MM WE. Center-Bottom: the quadruplet structure of a sectors: 4 + 4 inner MM layers (red) and 4 + 4 sTGC outer layers (blue). Right: the four different kind of MM quadruplets. Copyright 2020 CERN for the benefit of the ATLAS Collaboration. CC-BY-4.0 license.

In figure 4 the principle of operation of a MM is shown. A NSW MM layer is composed by a drift gap, 5 mm in thickness, where primary ionized electrons are drifted towards a mesh referred to ground and by the amplification gap, where the secondary ionization, provided by a ~ 4.5 kV/mm electric field, yields the avalanche collected by the resistive strips. The copper readout strips pick up the induced signal and make it available to the electronics.

Several challenges had to be faced in order to reach a set of stable operational conditions. The MM are particularly vulnerable to sparking, mainly because of the very narrow amplification gap: small fluctuations in the gap size could imply significant variations in the electric field and in a higher probability of sparking or low efficiencies. The solution for intermediate scale detectors was introduced with the *bulk Micromegas* concept [5]. The production procedure of a bulk MM allows

2020 JINST 15 C09019

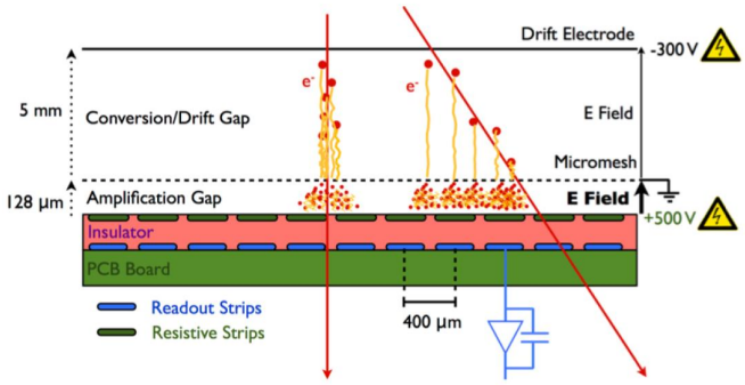

Figure 4. The principle of operation of a MM. A MIP produces primary ionization along its path through the drift gap. The electrons are then drifted by the electric field towards the mesh. The high electric field of the amplification gap gives rise to avalanches and provides a sizeble charge to be readout by the Front End electronics.

the mesh to be embedded into the readout PCB structure, reducing the probability of fluctuations in the gap size. Unfortunately this method cannot be applied to detectors of size bigger than 60 cm.

In order to scale the MM technology to the needs of the NSW upgrade, an R&D activity, called Muon ATLAS MicroMegas Activity (MAMMA) was started [6]. The spark issue was one of the main focuses of the activities of MAMMA. The best solution to the spark issue was found to be the use of a layer of resistive strips facing the amplification gap. The main results on the resistive strip readout studies can be found in [7].

In figure 5 the structure of a NSW MM readout panel is shown. A thin layer (50 µm) of insulator (kapton) hosts on top a pattern of interconnected resistive strips, deposited by screen printing technology. The typical resistivity of a strip is of the order of 10 MΩ/cm. Under the kapton foil a thin (25 µm) Akaflex glue layer hosts a pattern of copper strips, drowned into the glue substrate. The signals are induced through capacitive coupling to the readout strips. In case of a discharge occurs, the resistive strips are charged up and locally the electric field drops, dumping the current flow. The resistive and the copper strips follow the same geometrical pattern, with a 450(425) µm pitch for LM1/LM2 (SM1/SM2) quadruplets and 300 µm strip width. The resistive strip layer topology also includes a set of interconnections, with a typical alternate spacing of 1 cm, in order to allow a uniform resistance trough the panel surface. In figure 6 the interconnections between strips are visible. Each interconnection plays a role of a very low resistance between two adjacent strisp (few tenths of kΩ); along each strip the resistance between two interconnections is roughly 10 MΩ and it is due to the typical resistivity of the paste. While moving along a strip, the low resistance of the interconnections makes available an increasing number of parallel paths to the electrons moving towards the silver line, keeping the resistance almost uniform along any strip. The resistance gradient has been measured to be few kΩ/cm.

The spacing between the readout strip layer and the mesh is kept by a set of pillars, obtained by lamination of two Pyralux foils, each 64 µm thick, and by a subsequent photo-evaporation of the material excess around the pillars. This technique allows to define the size of the amplification gap, set to 128 µm. The shape of a pillar is a round-cornered rectangle, 1 mm × 300 µm in size.

2020 JINST 15 C09019

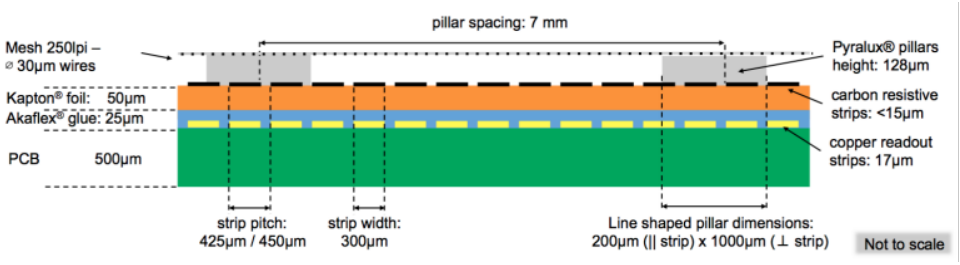

Figure 5. The PCB cross section of a readout panel. The copper strips are laying on a PCB, protected by a layer of glue. On top, a kapton foil provides the insulation with respect to the resistive strips, printed on it. Finally, spacing pillars provide the right size of the amplification gap to be kept through the detector surface.

In figure 6 a picture of a resistive strip readout panel and a magnified image of a pillar are shown. The pillars and the typical interconnection topology are clearly visible.

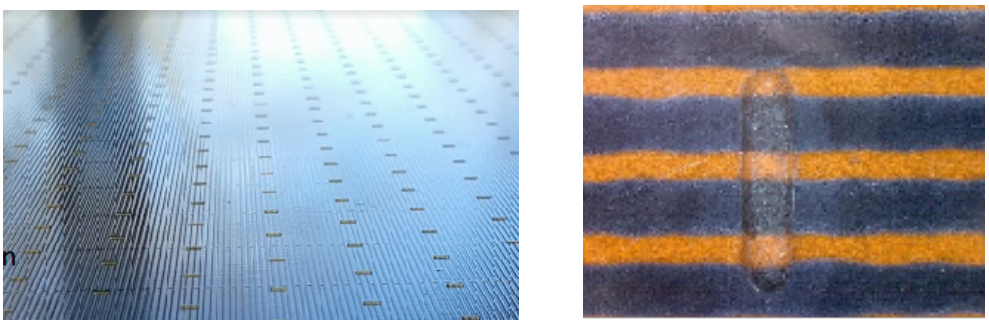

Figure 6. Left: a picture of a resistive strip readout panel: the pillars and the interconnection topology are clearly visibile to unaided eye. The spacing between pillars is 7 mm. Right: a pillar, 1 mm × 330 µm.

In figure 7-left the inner structure of a quadruplet is shown. A central double-side drift panel hosts a mesh on both sides. The mesh is glued and tensioned to the drift panel frame, that defines the 5 mm width of the drift gaps. Two double-side readout panels face the two central drift-panel meshes; finally, two single-side drift-panels face the external layers of the readout panels, while also closing the quadruplet. The four gaps, each composed by a 5 mm drift gap and a 128 µm amplification gap, are connected through a gas interconnection hole, allowing the gas flow through the whole quadruplet volume.

The electrical configuration of a drift+readout gap has been designed in order to simplify the quadruplet construction and to optimize the HV stability of the detector. The mesh, also connected to the drift frame, is referred to ground, in order to avoid applying HV to the detector frame. A positive potential (570 V in Ar/CO_2 93/7 gas mixture) is applied to the resistive strip readout plane. The field lines therefore close on the resistive strips and optimize the discharge protection through the local voltage drop on the strips.

In figure 7-right plot the coordinate system provided by a quadruplet is shown. The first two layers show strips orthogonal to the pseudorapidity coordinate (η strips) while the last two are inclined by 1.5° with respect to the firsts, providing the second coordinate (*stereo* strips).

2020 JINST 15 C09019

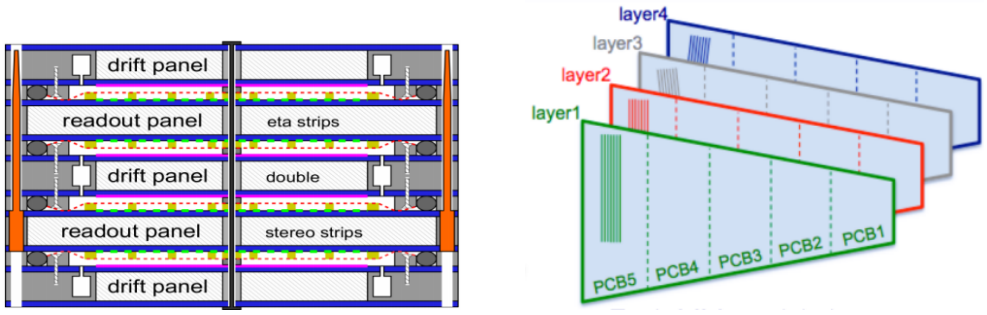

Figure 7. Left: the cross section of a quadruplet. An inner double-side drift panel faces on both side a double-side readout panel. Two outer single-side drift panels face the outer sides of the double-face readout panels. Right: the four layers of a quadruplet are composed by 3 (LM1/LM2 quadruplets) or 5 (SM1/SM2 quadruplets) PCBs. The layers provides two *eta*-aligned coordinate readout panels and two *stereo* coordinate readout panels. Copyright 2020 CERN for the benefit of the ATLAS Collaboration. CC-BY-4.0 license.

In figure 8 a picture of an SM1 readout panel is shown. The construction of gaps and drifts, their test and validation at the construction sites, prior the expedition to CERN, is discussed in section 3.

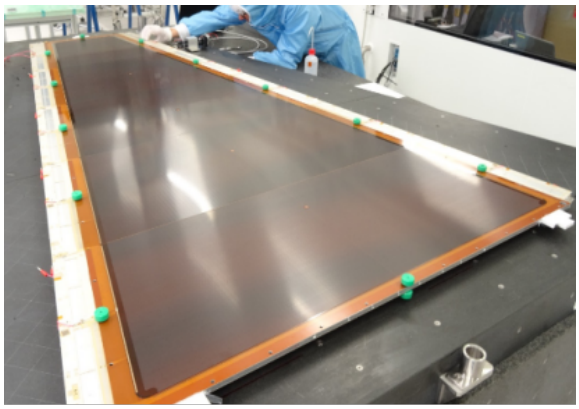

Figure 8. An SM1 readout panel. Each SM1/LM1 readout panel is composed by 5 different PCBs with increasing size (see section 3). Copyright 2020 CERN for the benefit of the ATLAS Collaboration. CC-BY-4.0 license.

3 Modules construction and tests

The NSW large sectors are equipped by large MM Double Wedge (LDW), while the small sectors by small DW (SDW)) (see figure 3). As already mentioned in section 2 each WE is segmented along pseudorapidity coordinate into two MM quadruplets. There are four types of MM quadruplets. The SDW are composed by SM1 and SM2 quadruplets, built in Italy and Germany, respectively. The LDW are composed by LM1 quadruplets, built in France, and by LM2 quadruplets built in Russia and Greece. All quadruplets have trapezoidal shapes with typical sizes between 2 and 3 m^2.

The construction of a quadruplet is a complex procedure, involving several steps and requiring high mechanical precision and a clean environment: this is done in order to avoid dirt or damages

2020 JINST 15 C09019

degrading the final resolution and/or the electrical stability of a quadruplet. A set of tests during the construction and before the delivery to CERN are also performed, in order to provide a first validation of the quadruplets.

The three drift panels, a central double drift and two outer single drifts, and the two double readout panels follow different production chains. The drift panels are glued to an aluminum frame while laying on a granite table (see figure 9-left), providing a planarity better than 20 µm. Subsequently, one or two cylindrical support structures are installed (figure 9-center) in order to fix the drift gap size to the desired 5 mm value. They also support the gas interconnection holes for providing the gas distribution through the whole quadruplet once mounted. Finally the mesh is glued and tensioned on the aluminum frame (figure 9-right).

The readout panels are mounted on a precision stiffback, composed by 3(5) aluminum plates with a required accuracy of 20 µm (see figure 10-right). The 3(5) PCBs are aligned on the stiffback and their relative position is measured by a CCD reading a Rasnik mask (figure 10-right), while the final planarity is measured by a laser. The 3(5) PCBs are then glued by a glue-distribution machine, together with the aluminum frame and the honeycomb, providing the required stiffness and also a ground reference to the final panel (see figure 11).

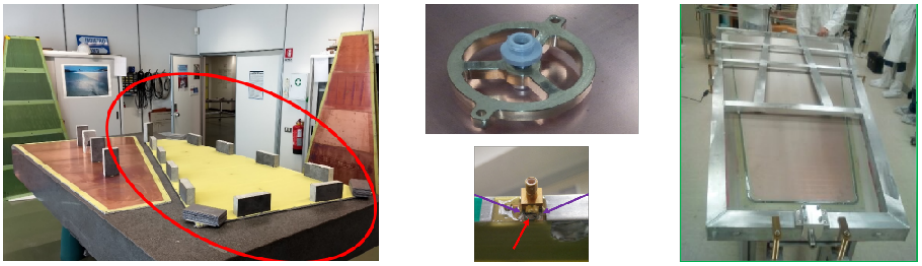

Figure 9. The drift panel finalization procedure. Left: the drift panels are glued to the frame. Center: top — gas interconnection between layers; bottom — high voltage connector. Right: the mesh is glued to the frame and tensioned. Copyright 2020 CERN for the benefit of the ATLAS Collaboration. CC-BY-4.0 license.

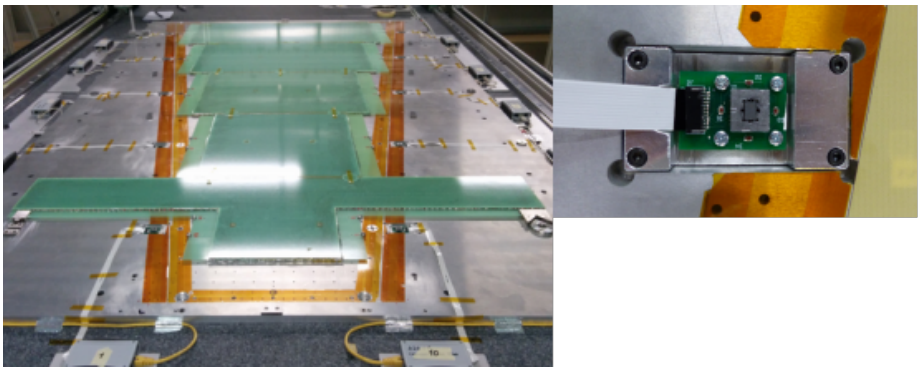

Figure 10. First steps of an SM1 quadruplet readout panel mounting. Left: the alignment structure (green) is mounted to subsequently host the 5 PCBs on a precision stiffback. Right: a CCD reading a Rasnik mask; the out-of-plane planarity is based on the stiffback planarity and measured by a laser (see text). Copyright 2020 CERN for the benefit of the ATLAS Collaboration. CC-BY-4.0 license.

2020 JINST 15 C09019

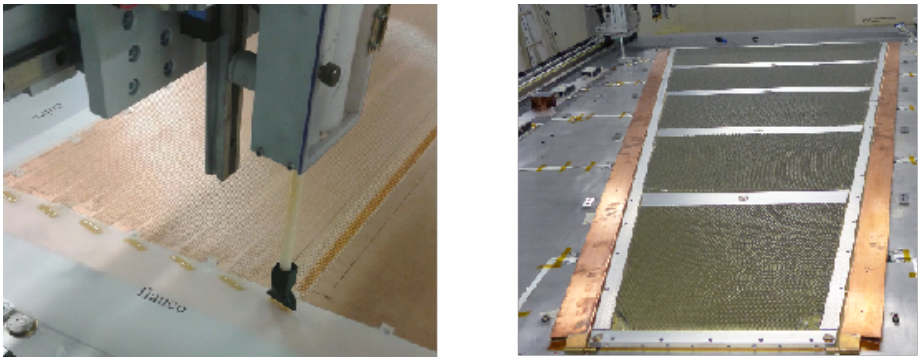

Figure 11. Construction of the readout panel. The 5 PCBs are glued using an automatic system, together with the aluminum frame and the metallic honeycomb. Copyright 2020 CERN for the benefit of the ATLAS Collaboration. CC-BY-4.0 license.

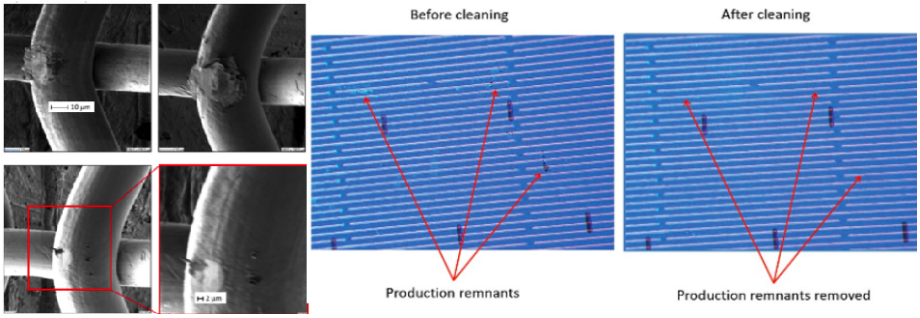

Figure 12. Left: a mesh at the microscope: imperfections are clearly visible. Right: dirt on a readout panel before and after the cleaning procedure. Copyright 2020 CERN for the benefit of the ATLAS Collaboration. CC-BY-4.0 license.

Drifts panels and readout panels are then assembled together into the final quadruplet. Before the final assembly the panels are deeply cleaned through dedicated procedures, in order to remove any residual, dust or grease, potentially harming the performances of the final quadruplet. In figure 12-right is shown a readout panel before and after the cleaning procedure, while the left picture shows imperfections of the mesh. The readout panels are brushed with both hard and soft brushes, using CIF as a detergent; they are then washed with demineralized water and dryed in a ventilated oven at 40°. The mesh is polished with 2500 sandpaper in order to remove any imperfection or metallic remnants, then washed with hot water at 40–45°, brushed with a mixture of water and NGL as a degreaser, and finally rinsed with demineralized water.

3.1 Tests and Construction Site validation

The main tests carried out during the construction procedure and after the final assembly are related to mechanical precision, gas tightness and high voltage stability of the quadruplets.

The 8 measurement planes of a MM DW with a resolution of 100 µm per plane, requires a high accuracy in positioning the readout strips; along the precision coordinate it should be better than 30 µm while the position of each plane through the Z coordinate should be better than 80 µm. In figure 13 a set of mechanical precision results are shown. The top plot reports the RMS of a set of ~

2020 JINST 15 C09019

130 LM1 single-panels thickness measurement. The average value of the RMS is 20 µm, well within the requirements. The alignment between the 4 panels of a quadruplet and their mutual orientation are also measured, by reading a set of 4 Rasnik masks in-built in the panels. The bottom-left plot shows the RMS of both the mutual alignment and the rotation for a set of 10 LM1 quadruplets: they are better than 50 µm and 50 µrad, respectively. Finally the bottom-right plot shows an LM2 final quadruplet thickness distribution, with a typical RMS of 117 µm, close to the requirements.

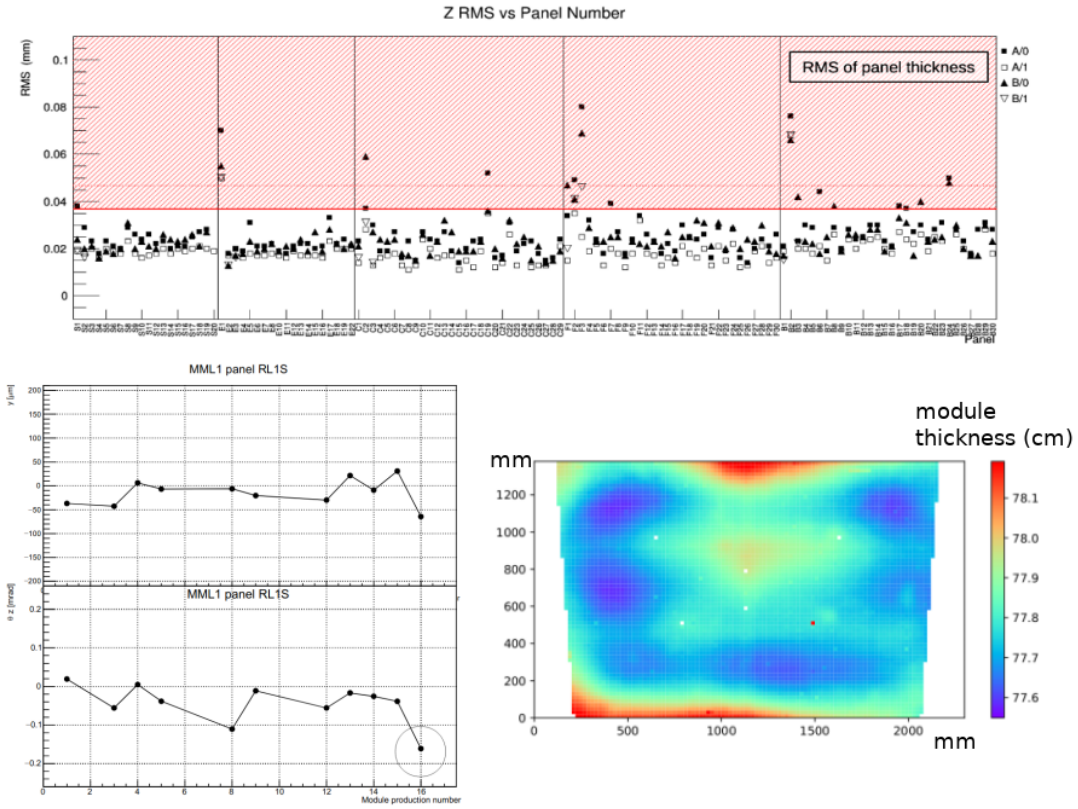

Figure 13. A set of mechanical precision measurements. Top: single panels thickness RMS for a set of more than 130 LM1 readout panels, showing an average value of 20 µm. Bottom left: alignment (overall shift and overall angle) for the first 10 LM1 quadruplets built. The last quadruplet (circled) is the only slightly out of specs. Bottom right: the thickness distribution of a final LM2 quadruplet (in mm): the RMS is 117 µm.

A finalized quadruplet is then flushed with standard gas mixture and slowly conditioned by rising the high voltage to the nominal value (570 V in Ar/CO_2 93/7). The conditioning procedure is a fundamental step for reaching stable operation conditions and for identifying any HV instability that may occur. Once the conditioning is completed the efficiency of the quadruplet is measured at the construction site by tracking cosmic rays. The measurement is performed by using APV25 as readout electronics and scintillators for providing the external trigger. A 35 cm Fe layer is used to cut muons at 0.5 GeV threshold. A picture of the LNF Cosmic Ray Stand and the 2D efficiency map of a layer of an SM2 quadruplet as measured with the cosmic ray stand of LMU are shown in figure 14.

2020 JINST 15 C09019

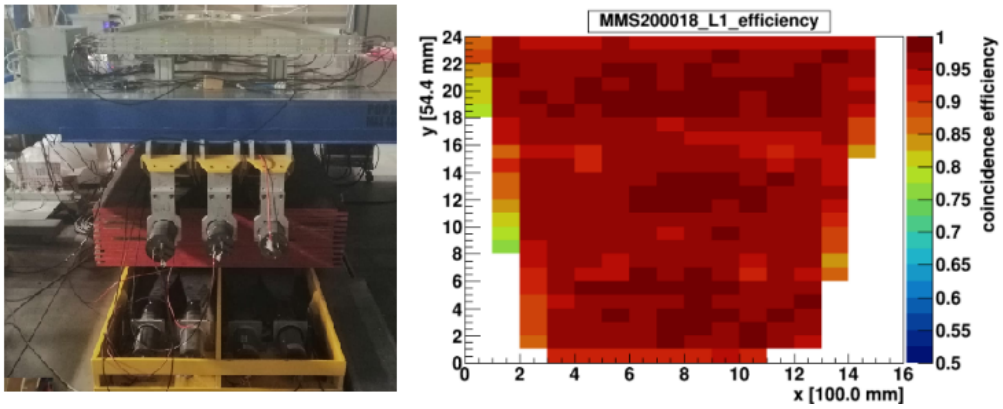

Figure 14. The Cosmic Ray Stand at INFN National Frascati Labs (Rome) and a typical efficiency distribution measured on a SM2 layer at the LMU (Munich). Copyright 2020 CERN for the benefit of the ATLAS Collaboration. CC-BY-4.0 license.

4 Modules Test, validation and integration at CERN

The integration of MM quadruplets into DWs is performed at CERN, where a complex chain of validation activities and tests are carried out on the new modules delivered by the four construction sites. The validation chain is meant to check the fundamental working parameters and performances of the new quadruplets, prior to the mechanical integration into DWs and the subsequent services installation and final checks. A scheme of the integration workflow is shown in figure 15. Once received a quadruplet undergoes two main tests: the gas tightness and the HV stability. The gas tightness measurement system has been designed in order to reach a sensitivity better than the ATLAS NSW leak rate limit, set to $10^{-5}\times$Volume l/min. The leak test approach is based on the differential measurement between the input and the output gas flow to a quadruplet. The system is calibrated by using a set of high precision needles and the data set is corrected in terms of temperature variations. A detailed description of the gas tightness system and procedure is given in [8].

Once a quadruplet passed the gas tightness test it is flushed with standard gas mixture until the relative humidity (RH) is measured to be lower than 12. A low RH value is a fundamental parameter for a stable working condition, since higher RH values trigger discharges and slowly drifting dark currents. The operational gas flow will be therefore defined according to the ATLAS environment parameters in order to keep the RH values within the working range.

The second validation step is the HV stability check. The HV stability showed to be the crucial parameter to be reached in order to get the NSW MM detectors working on long time scales and in a high radiation environment. The HV distribution and partitioning of the MM quadruplets is organized in 10 sections per layer for the SM1 and LM1 modules and in 6 sections per layer for the SM2 and LM2 modules: in total an SM1/LM1 quadruplet shows 40 HV sections while SM2/LM2 quadruplets has 24 HV sections. A Detector Control System (DCS) has been designed and implemented in order to allow the indipendent ramping of any of the 40(24) sections of the quadruplets under test. The HV test facility is composed by 4 HV nodes, allowing the test of 4 MM quadruplets at the same time. The nodes are powered by CAEN A7038DP HV boards, 1 kV–100 µA, the same used to power the MM DWs in ATLAS. During the HV test each quadruplet HV section

2020 JINST 15 C09019

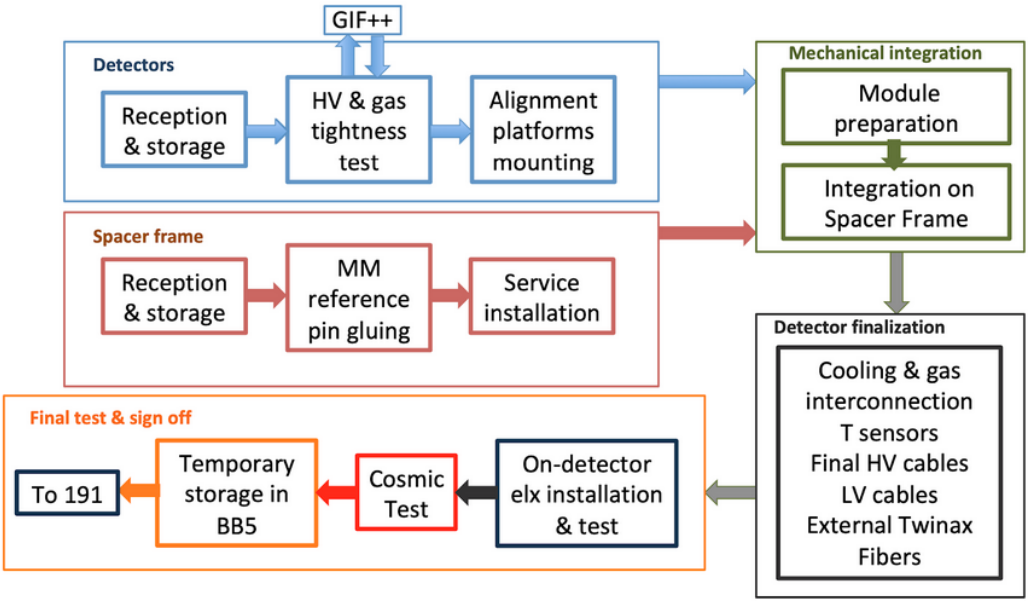

Figure 15. A scheme of the integration workflow from quadruplets to the final DWs. Copyright 2020 CERN for the benefit of the ATLAS Collaboration. CC-BY-4.0 license.

is ramped up to nominal HV, where feasible, with a defined ramping procedure, in order to keep dark currents below the 50-100 nA level and avoiding sections start discharging and potentially damaging the detector. The maximum HV value applied to a section is defined as the maximum value allowing to keep the spark rate below 6 spark/min and the dark current below 50-100 nA. A quadruplet is accepted for integration whenever the maximal HV configuration is reached and its estimated average efficiency reaches the 90 threshold value. The quadruplet estimated efficiency is defined as the average efficiency through the 40(24) sections, evaluated per each section by using a reference efficiency-HV curve measured using a pion beam at CERN [9]. If the efficiency is below 80 the quadruplets is sent back to the construction site while for intermediate values the module is sent to CERN GIF++ irradiation facility for further studies.

GIF++ facility [10] is a bunker equipped with a ^{137} Cs source, providing a gamma irradiation field with a peak at 667 keV and a total flux of 14 TBq. By using a set of absorbers it is easy to test MM chambers in a radiation environment close to the expected low energy γ background in ATLAS. In figure 16 the GIF++ radiation field is shown for both the downstream (right) and upstream (left) areas. The MM modules are tested at three independent HV nodes. Two nodes are used to investigate standard detectors with estimated efficiencies between 80 and 90; the position of these two standard nodes within the GIF++ facility allows to reach an average rate of 10 kHz/cm^2, close to the maximum rate expected in ATLAS in the high rapidity region. In figure 17 a typical result of a GIF++ standard test is shown. On the left a typical source scan shows the expected currents steps for different attenuation filters; the right plot shows the linearity response for several HV sections as a function of the incoming photon rate.

The GIF++ facility is also playing a central role for studying NSW MM chambers behaviour when exposed to long term radiation and for investigating new gas mixtures. Studies are ongoing and results will be available within few months.

2020 JINST 15 C09019

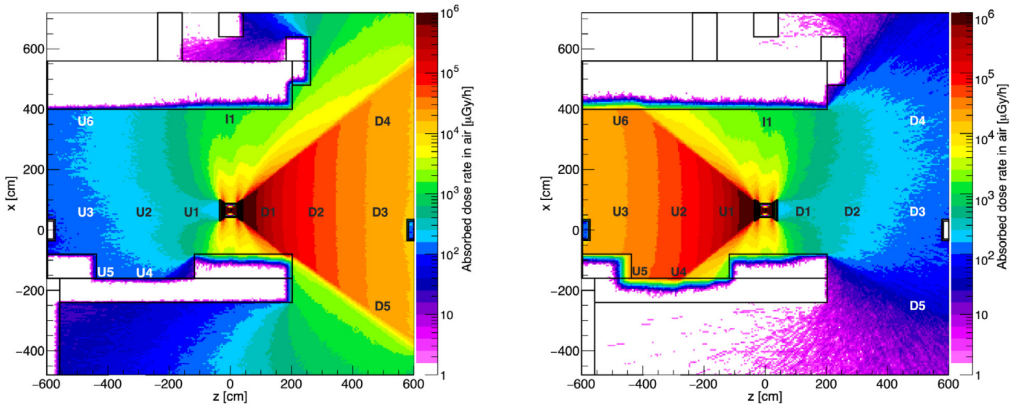

Figure 16. The GIF++ radiation fields in the upstream (left) and downstream (right) areas [10]. Copyright 2020 CERN for the benefit of the ATLAS Collaboration. CC-BY-4.0 license.

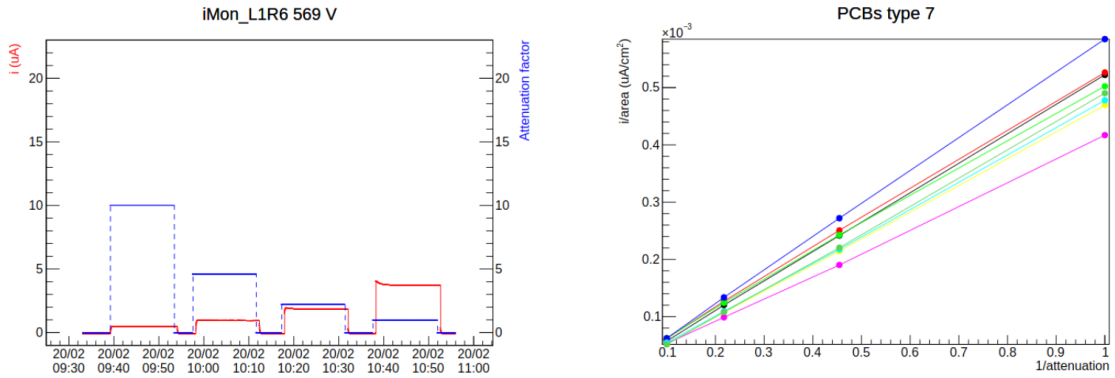

Figure 17. A typical set of measurement for the validation of MM quadruplets at the GIF++. Left: currents (red) vs attenuation filters (blue). Right: currents vs photon rate linearity for a set of HV sections of a MM quadruplets. Copyright 2020 CERN for the benefit of the ATLAS Collaboration. CC-BY-4.0 license.

After the HV/GIF++ validation, in-specs quadruplets undergo a set of steps for the installation of the alignment platforms, needed to keep the required mechanical precision when installed on the DWs and then on the NSW. A set of optical fibers and light sources are mounted on precision platforms, glued on the outer η layer of the quadruplet. The mechanical support of the NSW, the JD, is equipped by alignment bars, where a set of probes read the light sources (see figure 18-left). On top of the η layer of the quadruplet a set of Rasnik masks are glued (see figure 18-right), in addition to the light sources. The relative displacement of the Rasnik masks with respect to strips and light sources is known with high precision: this allows to map the absolute positions of the strips within the whole NSW.

A MM DW is composed by 2 WE (see section 1), supported by a spacer frame (SF) also hosting the routing of the data cable (Twinax). The mechanical and services integration is a complex procedure, where several steps are performed in order to get a DWs ready for the final tests and validation. The 4 quadruplets composing the DWs are equipped with all the services (HV, LV, data readout optical fibers, temperature sensors) and mechanical reference pins for structure

2020 JINST 15 C09019

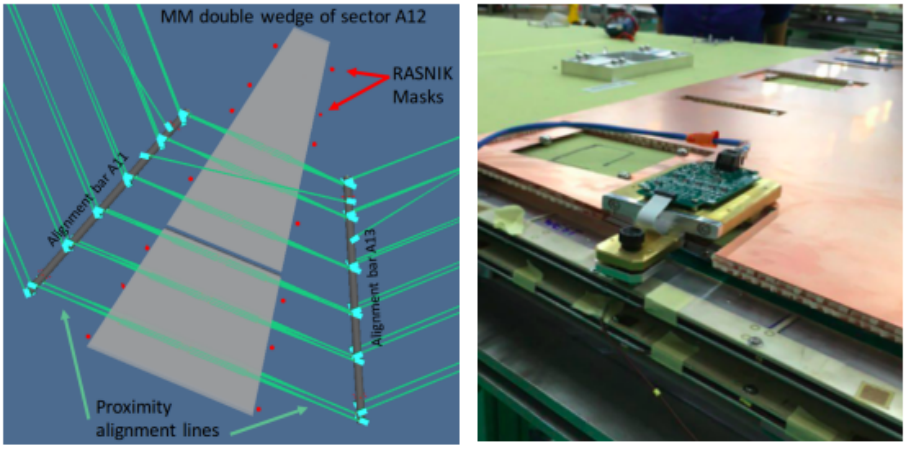

Figure 18. Left: the NSW alignment system, with the light sources mounted on the outer layers of MM DWs, read by light probes installed on the alignement bars. Right: Rasnik masks on the MM quadruplets allows the monitoring of the relative displacement between NSW bars and readout strips position. Copyright 2020 CERN for the benefit of the ATLAS Collaboration. CC-BY-4.0 license.

and readout electronics. Two quadruplets (SM1 and SM2 or LM1 and LM2 types) are mounted on one SF side and, once secured, they are flipped in order to allow the mounting of the second pair of quadruplets: the resulting DW, fully equipped, is then sent to the cosmic stand for electronics mounting, DAQ chain test and efficiency measurement with cosmic rays. In figure 19 two steps of the mechanical and services integration procedure are shown: a spacer frame mounting on a pair of quadruplets (WE) and the final DWs with services ready for the cosmic stand test.

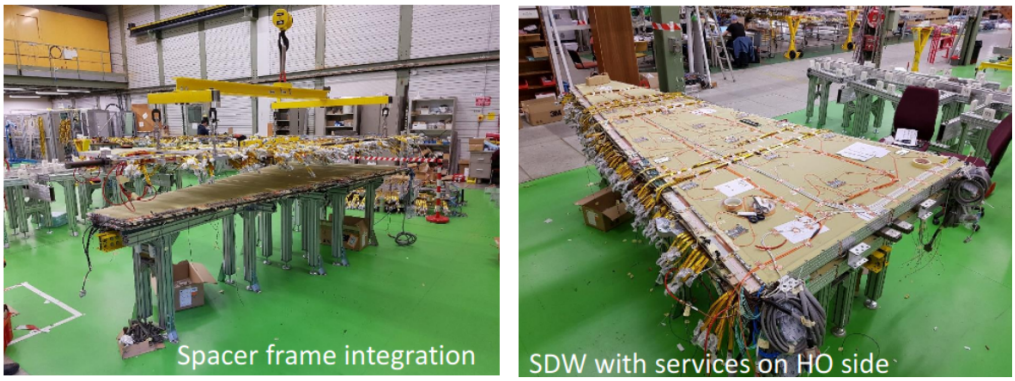

Figure 19. Two steps of the DW mechanical integration: a spacer frame while being mounted on a WE (left) and a fully equipped DW ready for cosmic ray test (right). Copyright 2020 CERN for the benefit of the ATLAS Collaboration. CC-BY-4.0 license.

The readout and trigger electronics is installed once the DWs are already hosted in the cosmic ray stand. Three different kinds of electronic cards have to be installed onto the DW. The MMFE8 card, providing the readout of half of the 2048 strips (the second half is readout by a MMFE8 installed on the opposite side of the PCB) of a readout panel and first level trigger information, is connected to the readout copper strips by a zebra connector. The MMFE8 card is hosting chips based

2020 JINST 15 C09019

on the VMM technology, a custom ASIC where each channel connects to a detector readout element and performs charge amplification, discrimination and precise amplitude and timing measurements through Analog-to-Digital Converters (ADCs). A DW hosts 128 MMFE8 cards, requiring precise alignment (better than 50 μm) to the copper strips throught the zebra connector. A group of 8 front-end MMFE8 cards are connected to the Level-1 Data-Driver Card (L1DDC), a data aggregator board, sending the concentrated data-flow to the Front-End LInk eXchange (FELIX) via optical fiber at a speed of 4.8 Gbps. Finally a third card, the ADDC, is devoted to the trigger signal packaging and transmission. ART signals provided by 8 MMFE8 VMM chips are driven to the ART Data-Driver Card (ADDC); it deserializes the addresses from several VMMs, appends a 5-bit VMM geographical address, a Bunch Cross ID (BCID) timestamp and forwards the data packet to the MM Trigger Processor through optical fiber. A complete description of the NSW data and trigger chains is provided in [11–13].

The fully equipped DW is then tested at the cosmic stand, in order to set the best HV settings, to check the full data acquisition chain and measure the efficiency before the final integration with sTGCs into a NSW Sector. After the best HV configuration is found, a set of tests are performed on communication, noise levels, data taking chain, reconstruction and efficiency measurement. The last is done by using a set of external scintillators for trigger purposes. Figure 20 shows a DW ready for testing at the cosmic ray stand at CERN (top-left) and reports few examples of tests done on a MM DW. In the top-right plot a cosmic rays efficiency map for the uppermost layer is shown: besides the very good uniformity through the whole DW area one can notice the low efficiency of the 7th PCB, due to the lower HV applied to this section. This example points out to the most important issue encountered in scaling a non-bulk MM technology to large surface detectors: the HV stability, addressed in section 5. The bottom-left plots shows the electron noise charge standard deviation, scaling linearly with the strip length. Finally the bottom-right plots show the hit multiplicity and the layer multiplicity during cosmic ray datat taking: the excess at single layer multiplicity is due to the reduced scintillator geometrical acceptance.

In figure 21 the first two NSW Sectors, mounted on the mechanical support of the NSW A (first wheel), are shown. The complete integration chain of these Sectors have been tested, from mechanics, gas system and services integration to the HV and the first DAQ chain validation and measurements.

5 The HV stability: issues and improvements

The MM scaling to large surfaces, the use of a non-bulk MM layout and thin 128 μm gaps, may give rise to HV instabilities. The choice of a resistive strip anode readout was actually driven by the need of protecting the amplification gaps from discharges, that would naturally arise from various weak points of such a layout: mesh sagitta, dirt, resistivity related issues. In figure 22 an example of a stable HV section (left plot) and a discharging section (right plot) are shown. An unstable section often limits the operating HV to values lower than the working point, thus giving rise to a non negligible efficiency loss. These evidences, occurring on $\sim$ 10 of the HV sections, brought to a set of studies in order to investigate the main sources of such instabilities.

The first investigations were performed in order to find a possible correlation between dirt and defects of the resistive strips readout and the HV instabilities. Various cleaning procedures

2020 JINST 15 C09019

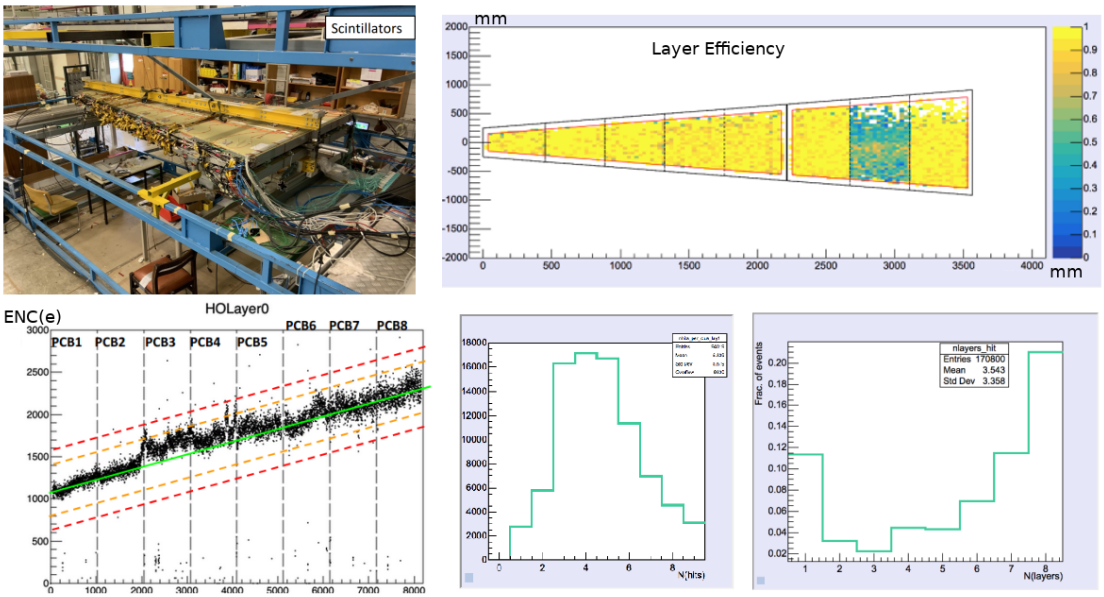

Figure 20. A set of tests on DW at the cosmic ray stand, prior to the final MM DW integration with the sTGC in a NSW Sector. Top-left: a DW ready for testing at the cosmic ray stand at CERN. Top-right: the efficiency map of the uppermost layer of the DW (the inefficiency shown on the seventh section is due to a lower voltage applied to the gap). Bottom-left: RMS noise linearity vs strip length. Bottom-right: hit multiplicity and layer multiplicity distribution (the peak at single layer multiplicity is due to the reduced acceptance of triggering scintillators). Copyright 2020 CERN for the benefit of the ATLAS Collaboration. CC-BY-4.0 license.

Figure 21. The wheel A of the NSW with the first two Sectors mounted. Copyright 2020 CERN for the benefit of the ATLAS Collaboration. CC-BY-4.0 license.

2020 JINST 15 C09019

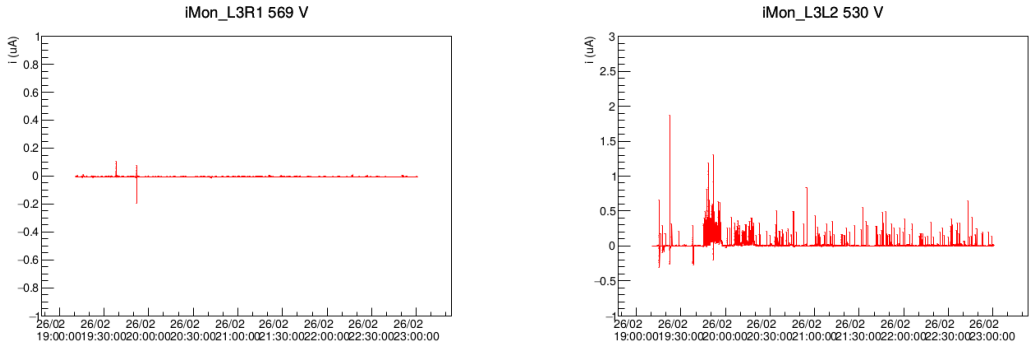

Figure 22. Left: a stable section, with a negligible dark current and almost no discharges. Right: a discharging HV section already at 53 V (−40 V w.r.t. the 570 V working point.) Copyright 2020 CERN for the benefit of the ATLAS Collaboration. CC-BY-4.0 license.

in addition to the standard cleaning previously described (see section 5) were tested on the strip readouts, in order to remove dirt around pillars and strip defects. Figure 23 shows examples of cleaning procedures. The top pictures shows a pillar before (left) and after (right) the cleaning by an ethanol bath: the residuals around the pillars are clearly removed. The bottom pictures show an SM2 readout panel while being cleaned by a NaOH bath (left) and a pillar after a brushing treatment with pumice powder (right). Even if all cleaning techniques showed good results in terms of dirt removal effectiveness, a clear correlation with improvements in HV stability was not found. All cleaning procedures showed partial improvements on the various readout panel layouts, but with no clear repeatibility or uniformity.

Among the various tests routinely performed during panels construction, one of the most important was the measurement of resistance between the HV distribution line and various regions of a readout panel. In figure 24-left the distribution of resistance measurements on a panel are reported. The red distribution is related to the measurements performed far from the coverlay, while the yellow one represents the region close to the coverlay. The resistance clearly decreases while approaching the coverlay and the left tail of the distribution shows resistance values well below 1 MΩ, a limit fixed for a stable HV operation. The right plot shows the minimum resistances for HV-stable readout panels (blue) and unstable panels (red); it is even more evident how HV-stable readout panels are related to higher minimum resistance values.

In parallel a set of long term irradiation tests were performed on a SM1 quadruplet at the GIF++ irradiation facility (see section 4). The chamber was exposed to an integral dose corresponding to that expected for 1 month of operation in ATLAS at high luminosity. After the long term test the quadruplet was reopened in order to visually check the displacement and the effects of discharges on the readout panel. In figure 25 pictures of the readout regions where discharges occured are reported. Discharges clearly happened close to the coverlay (right picture), a protection rim of pyralux between the HV distribution line and the active area (see section 3). Other discharges were found around the first strips interconnections, again close to the HV distribution line (left picture). These evidences confirmed the discharges were related to low resistance regions.

The source of low resistance weak points and areas has been investigated in order to find the best solution to the HV instability. The foil production procedure can play a role on the final

2020 JINST 15 C09019

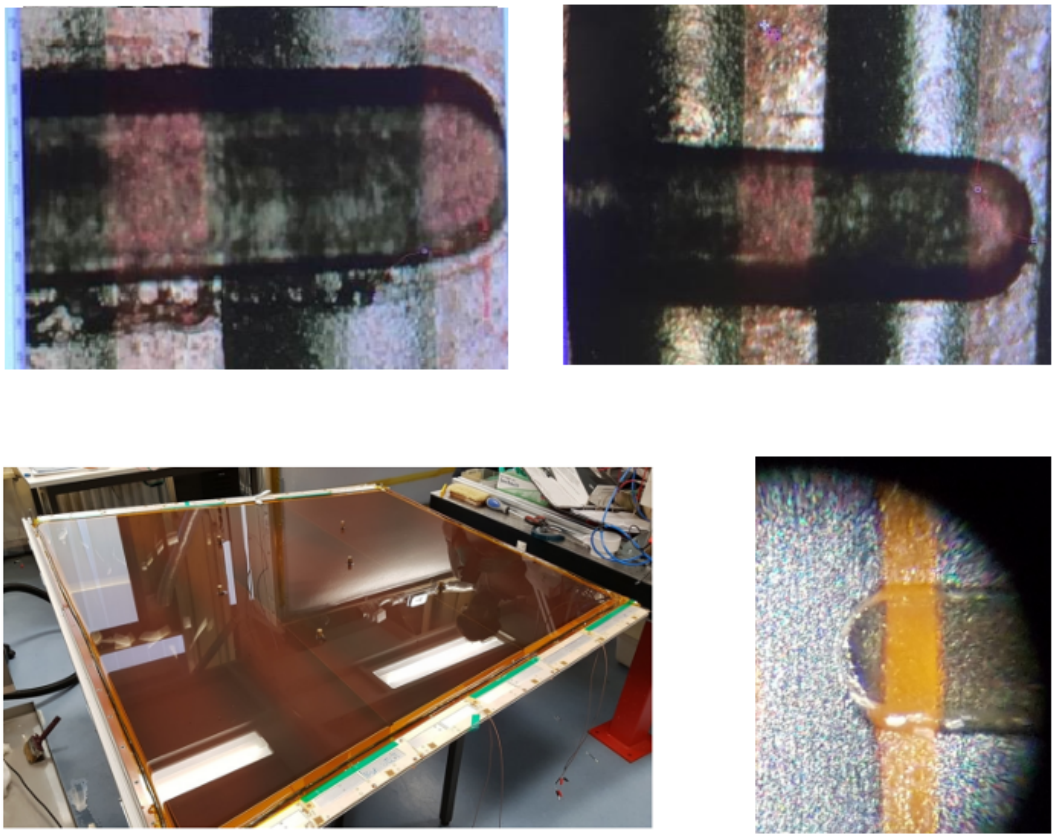

Figure 23. A set of alternative cleaning procedures. Top-left: a dirty pillar (1 mm × 300 µm). Top-right: the pillar after cleaning with an ethanol bath. Bottom-left: a readout panel being cleaned in a NaOH bath. Bottom-right a pillar after brushing with pumice powder. Copyright 2020 CERN for the benefit of the ATLAS Collaboration. CC-BY-4.0 license.

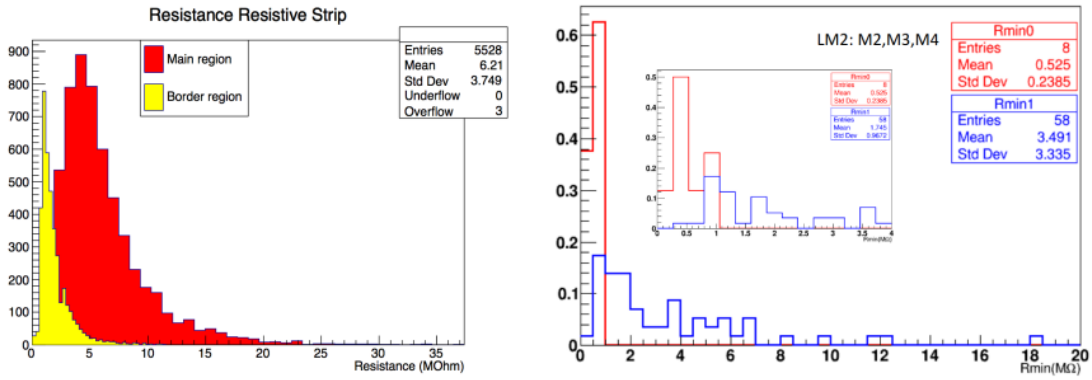

Figure 24. Readout panels resistance measurements. Left: distribution of resistance close to the coverlay (yellow) and at center of the readout panel (red). Right: minimum resistance distributions for HV-stable (blue) and for HV-unstable readout panels (red). Copyright 2020 CERN for the benefit of the ATLAS Collaboration. CC-BY-4.0 license.

2020 JINST 15 C09019

Figure 25. Pictures of a readout panel exposed to the equivalent dose of 1 month in ATLAS at high luminosity LHC conditions. Left: discharges residuals at strips interconnection zones. Right: discharges residuales close to the pyralux coverlay.

resistivity, acting also on uniformity and probability of defects. In figure 26 is shown the layering of a readout PCB applied during the foil production. The final resistivity depends on the material (Pacopad/Pacothane) as well as the production procedure, by varying the temperature, the pressure and the heating time. Several combinations of parameters are being tested in order to increase the final resistivity of the foil.

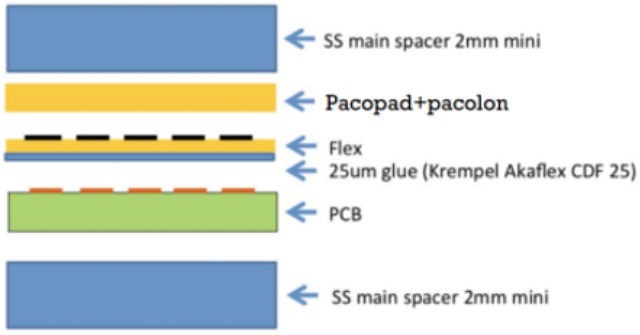

Figure 26. The layering of a resisitive foil.

The best procedure in order to stabilize the HV beahviour of low resistance readout panels was found to be the passivation of the weak area close to the coverlay. The aim of this action is to passivate the readout panel moving from the coverlay towards the inner region, until the resistance reaches 0.8–1 MΩ value. In figure 27 the passivation procedure is shown. The yellow area (bottom picture) represents the coverlay. A thin film of Araldyte ($\sim$ 100 µm) is deposited along the coverlay (top pictures); the width of such a passivation varies between the different readout panel layouts and resistivities, from 1 to 10 cm. Other chemicals are under study, such as Polyurethane, as an alternative solution to Araldyte. In figure 28 a typical result of passivation is shown. The values of resistance before and after the Araldyte layer deposit are shown; the final values stand between 0.7 and 1 MΩ.

2020 JINST 15 C09019

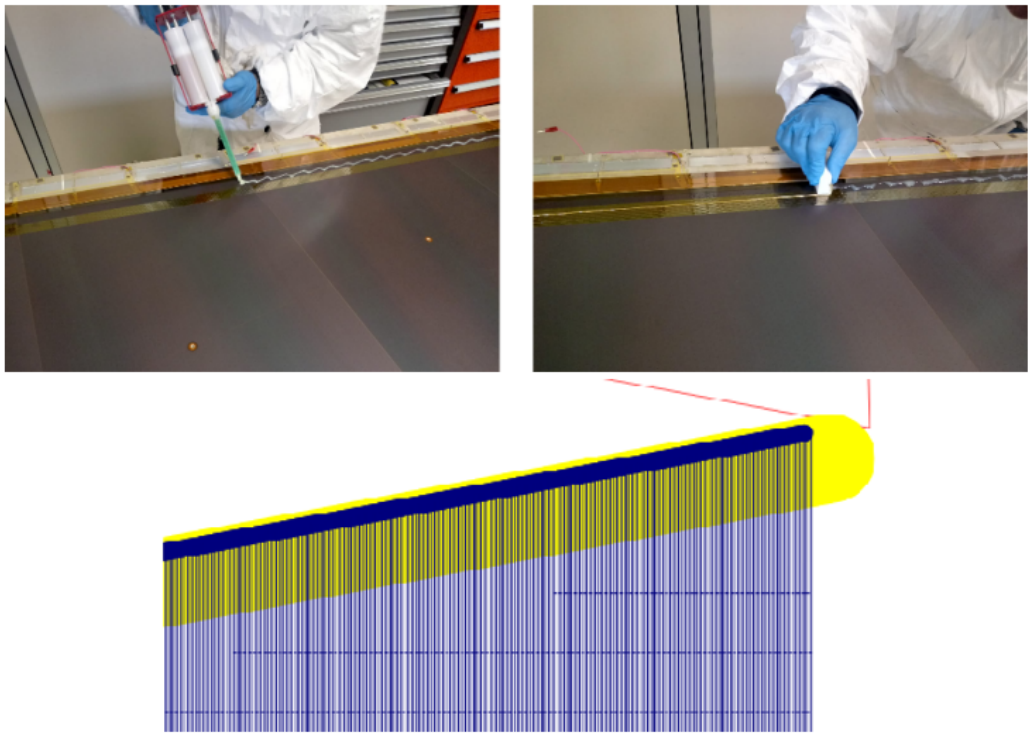

Figure 27. Top: the deposit procedure of the thin Araldyte layer. Bottom: the area interested by the passivation is a band close to the coverlay (yellow). Copyright 2020 CERN for the benefit of the ATLAS Collaboration. CC-BY-4.0 license.

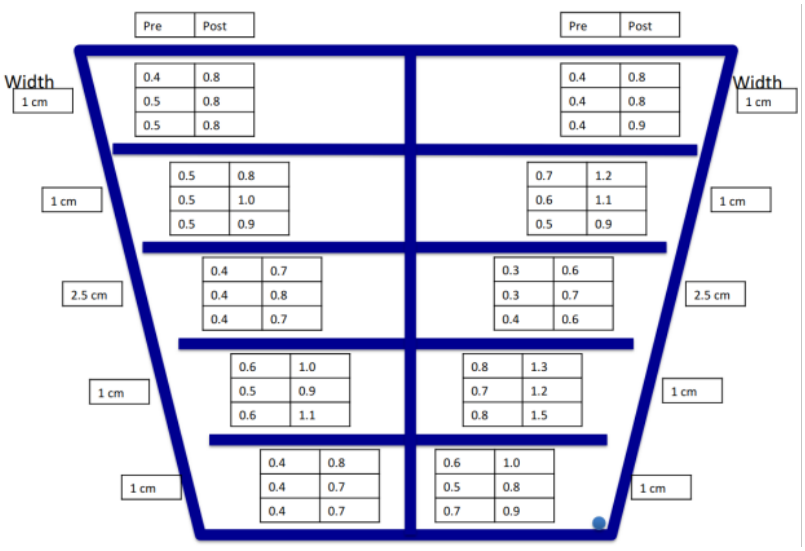

Figure 28. An example of resistance measurement taken on an SM1 Read-Out panel before (left value in tables) and after the passivation procedure (right value in tables). The reported values correspond to those measured close to the edge of the active region and are expressed in MΩ. Values outside the trapezoidal shape are the widths of passivated rims needed to reach the higher resistance values. Copyright 2020 CERN for the benefit of the ATLAS Collaboration. CC-BY-4.0 license.

2020 JINST 15 C09019

The passivation procedure was applied to a set of 33 quadruplets of any type. The passivation showed to be effective in recovering unstable HV sections. In figure 29 the fraction of stable HV sections for passivated and non passivated quadruplets are shown. The procedure brought to a clear improvement for all quadruplet types.

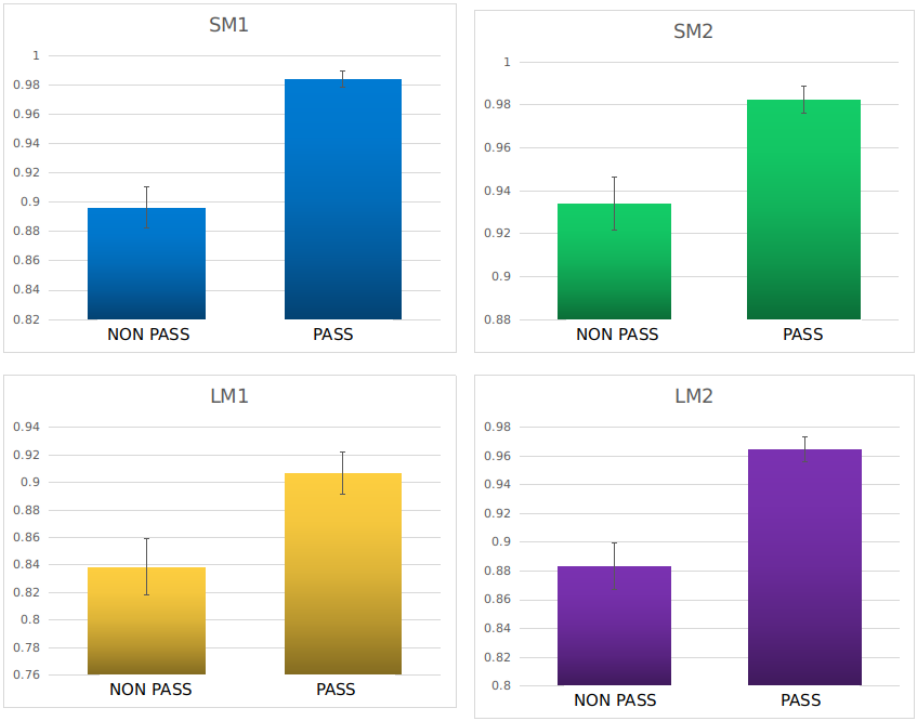

Figure 29. Fraction of stable HV sections for passivated and non passivated quadruplets.

Finally, studies on the mesh layout effects on the HV stability have also been performed. Dense, thin and calendered meshes have been found to be more stable in terms of discharges. A summary on the mesh studies can be found in [14].

6 Summary and conclusions

The ATLAS collaboration at LHC has developed a new large area muon station for the high luminosity upgrade in order to cover the high-rapidity region, with both triggering and tracking capabilities: the so called New Small Wheel (NSW). The technology chosen for tracking purposes was the resistive Micromegas technology, along with the small-strip Thin Gap Chambers (sTGC), mainly devoted to triggering. The R&D phase brought for the first time to the production of large area detectors based on this technology. The most sensitive parameter requiring investigations and studies was the HV stability: the resistive strip anode readout technology was chosen in order to protect the detector from potential discharges. The increase of the minimum resistance of the resistive readout panel was found to be crucial in order to stabilize the unstable HV sections ($\sim$ 10 of the whole production); the best approach was found to be the passivation with Araldyte of a band of few centimeters close to the HV distribution line, up to a minimum resistance of 0.8–1 MΩ. The

action was found to be very effective. At present 88 of the quadruplets needed for the first wheel (NSW A) have been produced and validated, and 75 of the final NSW A DWs have been integrated. Moreover, 25 of the quadruplets for the NSW C (second wheel) have been produced and validated for integration. MM DWs tested at the cosmic stand show good performances in terms of tracking capabilities. The whole integration chain from MM and sTGC DWs to NSW Sectors have been tested, up to the mechanical and services integration of two finalized Sectors on the NSW A support. First HV and DAQ noise tests were also performed on these Sectors, providing the first evidences that the detector works in its final coonfiguration. Final DAQ chain and trigger path activities and tests are ongoing to complete the Sectors integration into the NSW.

References

[1] ATLAS collaboration, *The ATLAS Experiment at the CERN Large Hadron Collider*, 2008 *JINST* **3** S08003.

[2] T. Kawamoto, S. Vlachos, L. Pontecorvo, J. Dubbert, G. Mikenberg, P. Iengo et al., *New Small Wheel Technical Design Report*, Tech. Rep., CERN-LHCC-2013-006, ATLAS-TDR-020 (2013).

[3] V. Smakhtin, G. Mikenberg, A. Klier, Y. Rozen, E. Duchovni, E. Kajamovitz et al., *Thin Gap Chamber upgrade for SLHC: Position resolution in a test beam*, *Nucl. Instrum. Meth. A* **598** (2009) 196.

[4] Y. Giomataris, P. Rebourgeard, J.P. Robert and G. Charpak, *MicrOMEGAs: A High granularity position sensitive gaseous detector for high particle flux environments*, *Nucl. Instrum. Meth. A* **376** (1996) 29.

[5] I. Giomataris, R. De Oliveira, S. Andriamonje, S. Aune, G. Charpak, P. Colas et al., *MicrOMEGAs in a bulk*, *Nucl. Instrum. Meth. A* **560** (2006) 405 [physics/0501003].

[6] J. Wotschack, *The development of large-area MicrOMEGAs detectors for the ATLAS upgrade*, *Mod. Phys. Lett. A* **28** (2013) 1340020.

[7] T. Alexopoulos, J. Burnens, R. de Oliveira, G. Glonti, O. Pizzirusso, V. Polychronakos et al., *A spark-resistant bulk-MicrOMEGAs chamber for high-rate applications*, *Nucl. Instrum. Meth. A* **640** (2011) 110.

[8] T. Alexopoulos, E. Gazis, S. Maltezos, A. Antoniou, V. Gika, S. Karentzos et al., *Gas system for the ATLAS NSW micromegas detectors: Design aspects and advanced validation methods for their QA/QC*, *HNPS Proc.* **24** (2019) 23.

[9] T. Alexopoulos et al., *Performance studies of resistive-strip bulk MicrOMEGAs detectors in view of the ATLAS New Small Wheel upgrade*, *Nucl. Instrum. Meth. A* **937** (2019) 125.

[10] D. Pfeiffer, G. Gorine, H. Reithler, B. Biskup, A. Day, A. Fabich et al., *The radiation field in the Gamma Irradiation Facility GIF++ at CERN*, *Nucl. Instrum. Meth. A* **866** (2017) 91 [arXiv:1611.00299].

[11] C. Bakalis, *Front-End and Back-End Electronics for the ATLAS New Small Wheel Upgrade*, *PoS* **ICHEP2018** (2019) 134.

[12] W. Wu, *FELIX: the New Detector Interface for the ATLAS Experiment*, *IEEE Trans. Nucl. Sci.* **66** (2019) 986 [arXiv:1806.10667].

[13] J. Wang, L. Guan, J.W. Chapman, B. Zhou and J. Zhu, *Design of a trigger data serializer ASIC for the upgrade of the ATLAS forward muon spectrometer*, *IEEE Trans. Nucl. Sci.* **64** (2017) 2958.

[14] O. Sidiropoulou, *Effect of mesh geometry on resistive MicrOMEGAs for the ATLAS experiment*, *J. Phys. Conf. Ser.* **1498** (2020) 012031, Tech. Rep., ATL-MUON-PROC-2019-004 (2019).

2020 JINST 15 C09019